batteries

MDPI

Article

Micro-Sized MoS_6@15%$Li_7P_3S_{11}$ Composite Enables Stable All-Solid-State Battery with High Capacity

Mingyuan Chang [1,2,3], Mengli Yang [1], Wenrui Xie [1], Fuli Tian [1], Gaozhan Liu [1], Ping Cui [1,4], Tao Wu [2,3,5,*] and Xiayin Yao [1,4,*]

1 Ningbo Institute of Materials Technology and Engineering, Chinese Academy of Sciences, Ningbo 315201, China
2 Municipal Key Laboratory of Clean Energy Technologies of Ningbo, University of Nottingham Ningbo China, Ningbo 315100, China
3 Department of Chemical and Environmental Engineering, University of Nottingham Ningbo China, Ningbo 315100, China
4 Center of Materials Science and Optoelectronics Engineering, University of Chinese Academy of Sciences, Beijing 100049, China
5 Key Laboratory of Carbonaceous Wastes Processing and Process Intensification of Zhejiang, Ningbo 315100, China
* Correspondence: authors: tao.wu@nottingham.edu.cn (T.W.); yaoxy@nimte.ac.cn (X.Y.)

Abstract: All-solid-state lithium batteries without any liquid organic electrolytes can realize high energy density while eliminating flammability issues. Active materials with high specific capacity and favorable interfacial contact within the cathode layer are crucial to the realization of good electrochemical performance. Herein, we report a high-capacity polysulfide cathode material, MoS_6@15%$Li_7P_3S_{11}$, with a particle size of 1–4 µm. The MoS_6 exhibited an impressive initial specific capacity of 913.9 mAh g^{-1} at 0.1 A g^{-1}. When coupled with the $Li_7P_3S_{11}$ electrolyte coating layer, the resultant MoS_6@15%$Li_7P_3S_{11}$ composite showed improved interfacial contact and an optimized ionic diffusivity range from 10^{-12}–10^{-11} cm^2 s^{-1} to 10^{-11}–10^{-10} cm^2 s^{-1}. The Li/Li_6PS_5Cl/MoS_6@15%$Li_7P_3S_{11}$ all-solid-state lithium battery delivered ultra-high initial and reversible specific capacities of 1083.8 mAh g^{-1} and 851.5 mAh g^{-1}, respectively, at a current density of 0.1 A g^{-1} within 1.0–3.0 V. Even under 1 A g^{-1}, the battery maintained a reversible specific capacity of 400 mAh g^{-1} after 1000 cycles. This work outlines a promising cathode material with intimate interfacial contact and superior ionic transport kinetics within the cathode layer as well as high specific capacity for use in all-solid-state lithium batteries.

Keywords: MoS_6@15%$Li_7P_3S_{11}$ composite; high capacity; interfacial contact; ionic transport kinetics; all-solid-state lithium battery

check for updates

Citation: Chang, M.; Yang, M.; Xie, W.; Tian, F.; Liu, G.; Cui, P.; Wu, T.; Yao, X. Micro-Sized MoS_6@15%$Li_7P_3S_{11}$ Composite Enables Stable All-Solid-State Battery with High Capacity. *Batteries* **2023**, *9*, 560. https://doi.org/10.3390/batteries9110560

Academic Editor: Yong-Joon Park

Received: 19 October 2023
Revised: 11 November 2023
Accepted: 15 November 2023
Published: 17 November 2023

1. Introduction

Commercial lithium-ion batteries have been utilized broadly in the fields of plug-in hybrid/electric vehicles, smartphones, laptop computers, and other portable electronic devices for the past several decades. They significantly reduce environmental pollution and greenhouse gas emissions. The energy densities of lithium-ion batteries are close to their limitation because of the low theoretical capacities of oxide cathodes (i.e., $LiFePO_4$, $LiCoO_2$, $LiMn_2O_4$, and $LiNi_xMn_yCo_zO_2$) and graphite anode materials [1]. Lithium–sulfur batteries that use lithium metal anodes instead of graphite can theoretically reach high specific capacity values [2]. However, there are safety concerns, such as leakage and risk of explosion, associated with organic liquid electrolyte-based lithium–sulfur batteries, and they exhibit poor rate capability and cycling stability due to the huge changes in the volume of sulfur that occur during the charge/discharge process. All-solid-state lithium batteries with nonflammable inorganic solid-state electrolytes have attracted considerable attention

in the field of energy storage [3–5]. Among the various solid electrolytes, sulfide solid electrolytes have broad application potential because of their high ionic conductivity and low elastic modulus. For example, the $Li_{10}GeP_2S_{12}$ sulfide solid electrolyte [6] possesses a high ionic conductivity of around 10^{-2} S cm^{-1} and surpasses the liquid electrolytes used in traditional lithium-ion batteries. The electrochemical stability of the Li_6PS_5Cl electrolyte was also investigated, and it displayed excellent stability when in contact with lithium metal [7].

Not only is the selection of the sulfide solid electrolyte essential, but the selection of an appropriate cathode material is also key to achieving high performance all-solid-state batteries. The classical oxide cathode materials and transition metal sulfides display different reaction mechanisms during the charge/discharge process. For classical lithium intercalation process in oxide cathode materials, because the 3d metal cationic band is much higher than the p band of oxygen, the ion–electron transfer reactions occur from lithium to the lowest unoccupied energy level of the transition metal d band in ionic oxides. The discharge/charge (lithium ion intercalation/de-intercalation) process relies on the d metal level to host/release the associated electrons; this is called the cation-driven redox process. For transition metal sulfide materials, the p band of sulfur is located in a higher position and is therefore closer or even penetrate the d band of transition metal. Due to the charge transfer of these two bands, the anionic redox process is triggered, and this can improve the reversible capacity of the battery [8]. The use of transition metal sulfides such as a-TiS_4 [9], FeS_2 [10], NiS_2 [11,12], and TiS_3 [12] in all-solid-state batteries has been widely studied due to the low cost of raw materials and their abundant yields. Meanwhile, their relatively high transport kinetics can promote conductivity and reduce charge transfer resistance. Furthermore, sulfide electrolytes show superior compatibility with transition metal sulfide cathodes due to their similar chemical potential, thus realizing high energy density [13,14]. However, all-solid-state lithium batteries with sulfide electrolytes and transition metal sulfide cathodes still suffer from inferior interfacial contact within the cathode layer.

Traditional sulfide cathode materials based on insertion reactions can accommodate lithium ions in their lattices without serious structural changes occuring during the intercalation/de-intercalation reaction of $xLi^+ + MS_y + xe^- \leftrightarrow Li_XMS_y$, in which M represents the transition metal [15]. Although insertion reaction-based cathode materials exhibit stability and long life cycles when used in all-solid-state lithium batteries, they still have intrinsic problems related to their limited space for lithium ions result in to a low specific capacity [8,16]. Nevertheless, in transition metal sulfide cathode materials with anionic redox driven chemistry (a-TiS_4 [9], MoS_3 [17], and FeS_2 [10]), sulfur fully or partially exists in the state of S_2^{2-} pairs, and this has a strong influence on specific capacity. For example, MoS_2 only has S^{2-} pairs and has a theoretical specific capacity of 670 mAh g^{-1} [18,19]. MoS_3 has both S_2^{2-} and S^{2-} pairs and has a higher theoretical specific capacity of 837 mAh g^{-1} [17]. The electronic structure of the S_2^{2-} group allows them to donate or receive electrons. Their ability as donors is attributed to the π^*_g orbital, which can release electrons that convert S_2^{2-} to S^{2-}. Because of the reversible reaction of $S_2^{2-} + 2e^- = 2S^{2-}$, multi-electron reactions proceed during the charge/discharge process, resulting in a high specific capacity [8,19]. In addition, transition metal sulfides with anionic redox driven chemistry display a high voltage plateau of about 2 V, which is close to that of a lithium–sulfur battery.

Even though MoS_2 and MoS_3 demonstrate high theoretical specific capacities, the actual reversible specific capacities of MoS_2 and MoS_3 in all-solid-state lithium batteries are only 592 mAh g^{-1} (0.1 C, 0.1–3.0 V) and 747 mAh g^{-1} (0.05 A g^{-1}, 0.5–3.0 V), respectively [19,20]. Ionic transport kinetics and interfacial contact within the cathode layer become crucial challenges. Coating a thin electrolyte layer onto the surfaces of active materials is an effectively strategy to enhance ionic transport kinetics and the contact between the solid electrolyte and the active material [17,21]. Compared with MoS_2 and MoS_3, MoS_6 is considered one of the most promising cathode materials for all-solid-state lithium batteries because of its ultra-high theoretical specific capacity of 1117 mAh g^{-1}, which is a result

of its high S_2^{2-} content as well as its amorphous nature, according to which possess open and random transmission paths to achieve cycling stability [22]. It therefore has potential applications in high energy all-solid-state batteries.

In this work, a micro-sized cathode material composite, MoS_6@15%$Li_7P_3S_{11}$, is designed for use in all-solid-state lithium batteries. First, MoS_6 was synthesized using a wet chemical method. After the in situ coating of the $Li_7P_3S_{11}$ solid electrolyte onto the MoS_6, the ionic diffusivity enhanced from 10^{-12}–10^{-11} cm^2 s^{-1} to 10^{-11}–10^{-10} cm^2 s^{-1}. The Li/Li_6PS_5Cl/MoS_6@15%$Li_7P_3S_{11}$ all-solid-state lithium batteries exhibited high initial and reversible discharge capacities of 1083.8 mAh g^{-1} and 851.5 mAh g^{-1}, respectively, at 0.1 A g^{-1} and 25 °C within 1.0–3.0 V. Because of the remarkable intimate interfacial contact between the active material MoS_6 and the solid electrolyte, these all-solid-state batteries can realize a long cycle life of 1000 cycles with a high reversible specific capacity of 400 mAh g^{-1} at 1 A g^{-1} and 25 °C.

2. Materials and Methods

2.1. Synthesis of $(NH_4)_2Mo_2S_{12}$

$(NH_4)_2Mo_2S_{12}$, which was used as a precursor, was synthesized using wet chemical methods. Briefly, 4.5 g of $(NH_4)_6Mo_7O_{24}{\cdot}4H_2O$ and 3 g of $NH_2OH{\cdot}HCl$ were dissolved in 60 mL of water (50 °C). Next, 12 g of sulfur powder and 60 mL of $(NH_4)_2S$ (6−20% aqueous solution) were mixed and stirred for 1 h. The two abovementioned solutions were mixed together and placed in an oven at 50 °C and 90 °C for 1 h and 4 h, respectively. After filtering, the filtrate was mixed with 20 mL of $(NH4)_2S$ and allowed to stand for 36 h. It was then filtered and washed with iced water, ethanol carbon disulfide, and iced diethyl ether. The obtained $(NH_4)_2Mo_2S_{12}$ displayed a crystal structure which matched the standard peaks in the PDF card (JCPDS: F73-0900) (Figure S1) [23].

2.2. Synthesis of Micro-Sized MoS_6

The micro-sized MoS_6 was prepared via an aqueous solution reaction corresponding to the reaction of $(NH_4)_2Mo_2S_{12} + I_2 = 2NH_4I + 2MoS_6$. Accordingly, 0.28 g of $(NH_4)_2Mo_2S_{12}$ and 0.2 g of iodine were separately dissolved in *N*,*N*-dimethylformamide. Afterward, the two solutions were thoroughly mixed together and stirred continuously for 30 min. The obtained MoS_6 was filtered, washed with *N*,*N*-dimethylformamide, CS_2, and acetone, and finally dried and stored in an argon atmosphere.

2.3. Synthesis of MoS_6@15%$Li_7P_3S_{11}$ Composite

A in situ liquid phase reaction and an annealing process were conducted in order to prepare the MoS_6@15%$Li_7P_3S_{11}$ composite [17]. The prepared MoS_6 was mixed with P_2S_5 and Li_2S powders and then underwent magnetic stirring in anhydrous acetonitrile at 60 °C for 12 h. After removing the residual solvent, the $Li_7P_3S_{11}$ precursor was in situ coated with MoS_6, and the precursor was then collected and heated at 260 °C for about 1 h to obtain the MoS_6@15%$Li_7P_3S_{11}$ composite.

Details concerning the synthesis of $Li_{10}GeP_2S_{12}$, Li_6PS_5Cl, and 75%Li_2S-24%P_2S_5-1%P_2O_5 can be found elsewhere. The ionic conductivities of these solid electrolytes were 8.27×10^{-3} S cm^{-1} ($Li_{10}GeP_2S_{12}$), 6.11×10^{-3} S cm^{-1} (Li_6PS_5Cl), and 1.54×10^{-3} S cm^{-1} (75%Li_2S-24%P_2S_5-1%P_2O_5).

2.4. Material Characterization

X-ray diffraction (XRD) measurements were conducted using a Bruker D8 Advance Davinci (Karlsruhe, Germany) with Cu *Kα* radiation of λ = 1.54178 Å in a 2*θ* range of 10–60° to determine the crystal structure of the samples. Raman spectra results were recorded in a range of 250 to 580 cm^{-1} using a Raman spectrophotometer (Renishaw inVia Reflex, Gloucestershire, UK) with a 532 nm laser. The atom ratio of the MoS_6 was analyzed via an inductively coupled plasma emission spectrometer analysis (ICP-OES, Spectro Arcos, Spectro, Dusseldorf, Germany). Field emission scanning electron

microscopy (SEM, S-4800, Hitachi, Tokyo, Japan) and field emission scanning electron microscopy energy dispersive spectroscopy (SEM-EDS, S-4800, Hitachi, Tokyo, Japan) were conducted using an accelerated voltage of 15 kV to confirm the morphology, particle size, and elemental distribution. High-resolution transmission electron microscopy (HRTEM) was performed using an FEI Tecnai F20 (Hillsboro, OR, USA) with an accelerated voltage of 200 kV to confirm the existence of the $Li_7P_3S_{11}$ solid sulfide electrolyte thin layer on the surface of the MoS_6. An electrochemical workstation (Solartron 1470E, Bognor Regis, UK) was employed to conduct cyclic voltammetry (CV) measurements and electrochemical impedance spectroscopy (EIS). All of the samples used for the various measurements were prepared in glove boxes, and all of the measurements were obtained at room temperature.

2.5. Assemby and Evaluation of All-Solid-State Lithium Batteries

To analyze the electrochemical performances of the synthesized samples described above, the obtained MoS_6, MoS_6@15%$Li_7P_3S_{11}$ composite, $Li_{10}GeP_2S_{12}$, and Super P were homogeneously mixed with a weight ratio of 40:50:10. For the preparation of the Li/Li_6PS_5Cl/MoS_6 all-solid-state batteries, Li_6PS_5Cl (150 mg) solid electrolyte pellets (ϕ = 10 mm) were fabricated via cold pressing at 240 MPa. The previously synthesized composite cathodes (~1 mg/cm^2) were then homogeneously spread onto the electrolyte surface and cold pressing was applied again at 240 MPa. Finally, metallic lithium foil with a 10 mm diameter was attached to the other side of the Li_6PS_5Cl layer at 360 MPa. For the purpose of comparison, Li/75%Li_2S-24%P_2S_5-1%P_2O_5/$Li_{10}GeP_2S_{12}$/MoS_6 all-solid-state batteries were fabricated as well. Bilayer pellets (ϕ = 10 mm) consisting of $Li_{10}GeP_2S_{12}$ and orthorhombic phase 75%Li_2S-24%P_2S_5-1%P_2O_5 were constructed at 240 MPa as well. The abovementioned cathodes were spread onto the sides of the $Li_{10}GeP_2S_{12}$ solid electrolytes homogeneously, and this was followed by cold pressing at 240 MPa. Pieces of metallic lithium foil (ϕ = 10 mm) were placed onto the sides of the 75%Li_2S-24%P_2S_5-1%P_2O_5 solid electrolytes by pressing them together at 360 MPa. The bilayer solid electrolyte pellets were necessary due to the instability caused by the side-reaction of the $Li_{10}GeP_2S_{12}$ and the lithium metal. All of these processes were carried out in a glove box with a dry argon atmosphere.

Galvanostatic charge and discharge tests were conducted at room temperature on a multi-channel battery test system under various current densities with voltages ranging from 1.0 V to 3.0 V. The galvanostatic intermittent titration technique (GITT) was used at 1 A g^{-1} for 1 min followed by a 120 min rest. The Li ion diffusion coefficient (D) was determined using Equation (1), which is based on the Fick's second law [24]:

$$D = \frac{4}{\pi\tau}\left(\frac{n_m v_m}{S}\right)^2\left(\frac{\Delta E_s}{\Delta E_t}\right)^2 \quad (1)$$

where τ is the duration of the pulse, n_m and v_m are the molar mass (mol) and volume (cm^3/mol) of the active material, respectively, S is the cell interfacial area, and ΔE_s and ΔE_t are the voltage drops of the pulse and discharge processes [25].

3. Results and Discussions

To better demonstrate the properties of the prepared sample, the Mo/S atom ratio was measured using an inductively coupled plasma emission spectrometer (ICP) (Table S1). The actual remaining weight ratios of the Mo and S were 31.5 wt% and 63.5 wt%, respectively, indicating an Mo/S ratio of 6.036, which is in agreement with the theoretical value of 6. The procedure for synthesizing the MoS_6@15%$Li_7P_3S_{11}$ composite is schematically illustrated in Figure 1. A $Li_7P_3S_{11}$ solid electrolyte precursor was in situ coated onto the MoS_6 surface during facile liquid phase deposition. After a 260 °C annealing treatment, the MoS_6@15%$Li_7P_3S_{11}$ composite was successfully prepared.

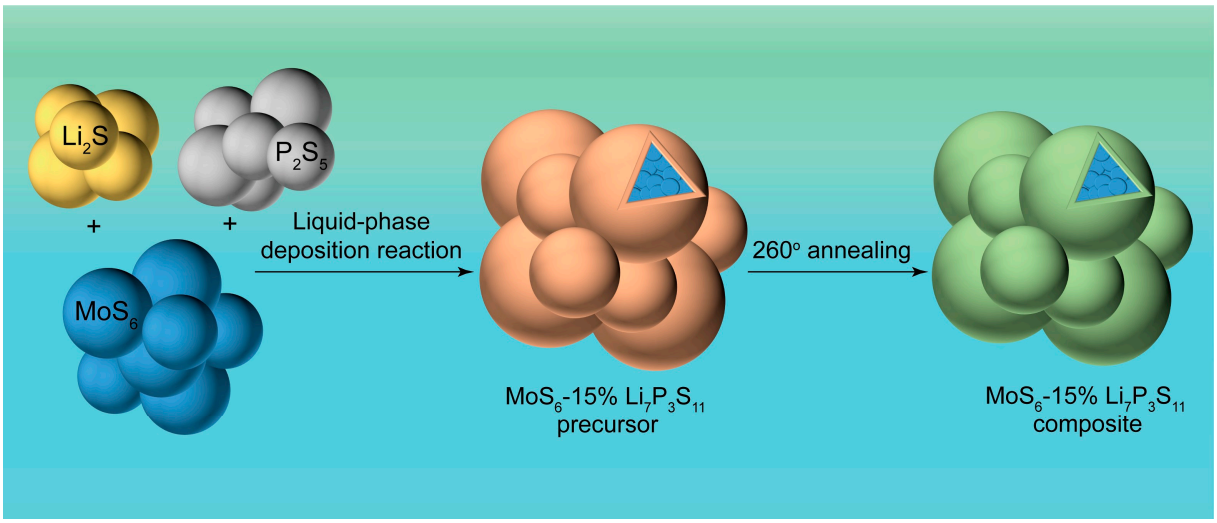

Figure 1. Schematic diagram of procedure for preparing MoS_6@15%$Li_7P_3S_{11}$ composite.

The XRD patterns of the MoS_6 and MoS_6@15%$Li_7P_3S_{11}$ composite are shown in Figure 2a, and they confirm the amorphous nature of MoS_6. No characteristic peaks were detected for the $Li_7P_3S_{11}$ sulfide electrolytes, indicating the low amount of $Li_7P_3S_{11}$ sulfide electrolytes in the coating layer. In order to confirm the existence of the $Li_7P_3S_{11}$ sulfide solid electrolytes in the MoS_6@15%$Li_7P_3S_{11}$ composite, Raman spectroscopy was performed (Figure 2b). The peaks located in the ranges of 286–385 cm^{-1} and 518–550 cm^{-1} correspond to vibrations of molybdenum sulfide bonds and bridging disulfide/terminal disulfide [26,27]. Furthermore, the peak located at 421cm^{-1} can be attributed to the PS_4^{3-} in the $Li_7P_3S_{11}$ sulfide solid electrolyte [21].

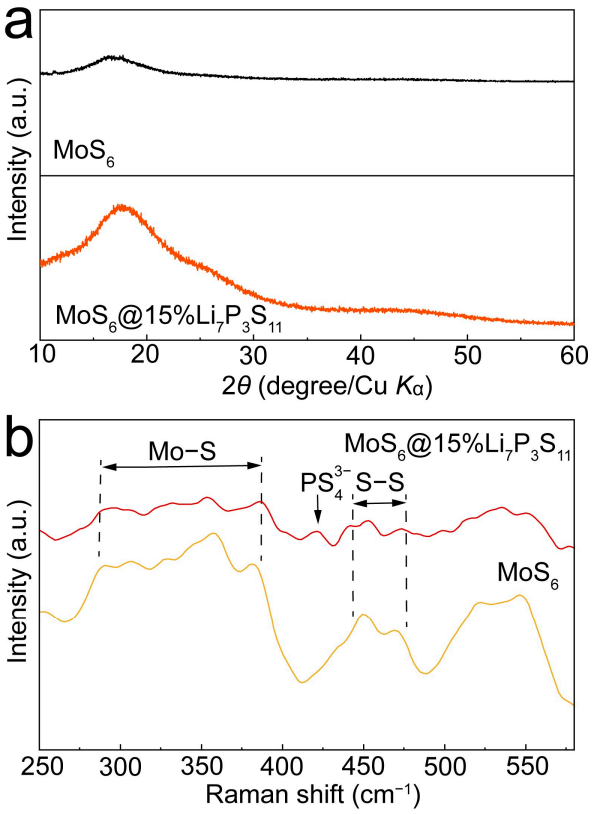

Figure 2. (**a**) XRD patterns of MoS_6 and MoS_6@15%$Li_7P_3S_{11}$ composite. (**b**) Raman spectra of MoS_6 and MoS_6@15%$Li_7P_3S_{11}$ composite.

The morphology and microstructure of the MoS_6 and MoS_6@15%$Li_7P_3S_{11}$ composite were observed using SEM and HRTEM (Figure 3). The particle sizes of the MoS_6 and MoS_6@15%$Li_7P_3S_{11}$ composite were in the range of 1–4 µm (Figure 3a,b). EDS mapping of the MoS_6@15%$Li_7P_3S_{11}$ composite clearly illustrates the good distribution of molybdenum (blue), phosphorus (purple), and sulfur (yellow) (Figure 3c). The HRTEM images further confirmed that $Li_7P_3S_{11}$ solid electrolytes were uniformly growing on the surface of the MoS_6 (Figure 3d,e), and this facilitates improvements in ionic transport kinetics and the formation of intimate interfacial contact. The *d*-spacings of 0.38, 0.35, and 0.309 nm correspond to the d_{030}, d_{202}, and d_{-211} spacing of the $Li_7P_3S_{11}$, respectively (Figure 3f) [21].

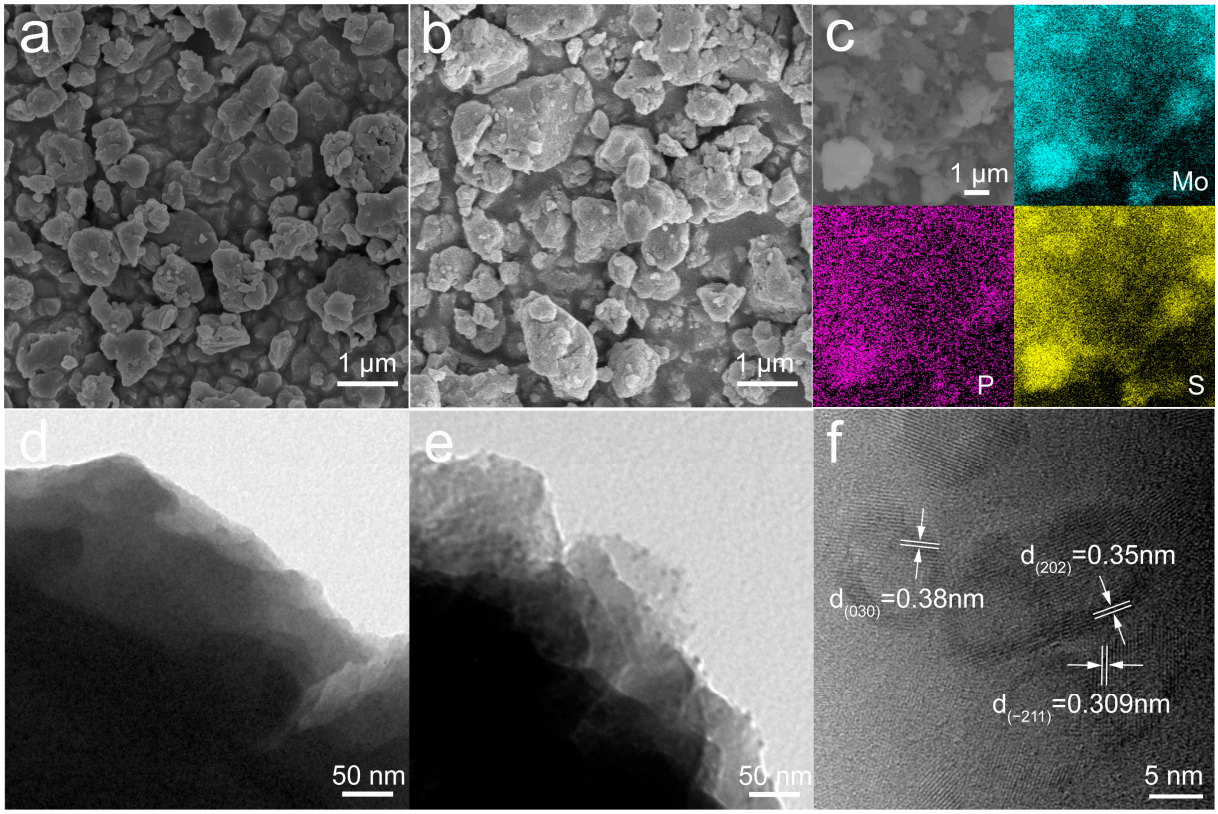

Figure 3. SEM images of (**a**) MoS_6 and (**b**) MoS_6@15% $Li_7P_3S_{11}$, EDS mapping of (**c**) MoS_6@15%$Li_7P_3S_{11}$ composite, TEM images of (**d**) MoS_6 and (**e**) MoS_6@15% $Li_7P_3S_{11}$, and HRTEM images of (**f**) MoS_6@15% $Li_7P_3S_{11}$.

The electrochemical performance of the MoS_6 was tested in all-solid-state lithium batteries. Two types of battery configuration were employed at 25 °C and 0.2 A g^{-1}, i.e., $Li/Li_6PS_5Cl/MoS_6$ and $Li/75\%Li_2S$-$24\%P_2S_5$-$1\%P_2O_5/Li_{10}GeP_2S_{12}/MoS_6$ all-solid-state batteries. As Figure S2 shows, the $Li/Li_6PS_5Cl/MoS_6$ all-solid-state battery exhibited a reversible specific capacity of 361.8 mAh g^{-1} after 200 cycles, which was higher than the value exhibited by the $Li/Li_{10}GeP_2S_{12}/75\%Li_2S$-$24\%P_2S_5$-$1\%P_2O_5/MoS_6$ all-solid-state battery (78.3 mAh g^{-1}), indicating a better capacity retention. For the purpose of comparison, cycles of $50MoS_6$:$50Li_{10}GeP_2S_{12}$, $40MoS_6$:$50Li_{10}GeP_2S_{12}$:10Super P, and $40MoS_6$:$40Li_{10}GeP_2S_{12}$:20Super P were performed at 0.1 A g^{-1} and 25 °C to determine the appropriate mixing ratio, as is shown in Figure S3. The capacity retention of the $40MoS_6$:$50Li_{10}GeP_2S_{12}$:10Super P was 544.8 mAh g^{-1} after 10 cycles; this was higher than the 394.69 mAh g^{-1} and 438.29 mAh g^{-1} values observed for the $50MoS_6$:$50Li_{10}GeP_2S_{12}$ and $40MoS_6$:$40Li_{10}GeP_2S_{12}$:20Super P, respectively, and indicated a high reversible discharge capacity.

To reveal the electrochemical reaction mechanisms of the MoS_6 and MoS_6@15% $Li_7P_3S_{11}$ composite, CV curves were generated for the $Li/Li_6PS_5Cl/MoS_6$ and $Li/Li_6PS_5Cl/$

MoS_6@15%$Li_7P_3S_{11}$ all-solid-state batteries for the first three cycles, and these are shown in Figure 4a,b. During the first cathodic scan, there was a reduction peak at around 1.75 V which can be attributed to the lithiation process of the MoS_6 and a further conversion process. During the initial anodic scanning period, the oxidation peak which occurred at 2.25 V corresponds to the de-lithiation processes and the forming of molybdenum sulfides. The CV curves of the MoS_6@15%$Li_7P_3S_{11}$ composite are similar to those of the MoS_6; they show the same electrochemical reaction process [21,28]. Even so, the redox peaks of the MoS_6@15%$Li_7P_3S_{11}$ composite are narrower and stronger than those of the MoS_6, illustrating enhancements in the reversibility and electrochemical reaction kinetics resulting from favorable ionic diffusion. In the second cycle, the CV curves display an apparent tendency to overlap, which indicates that the MoS_6@15%$Li_7P_3S_{11}$ composite has excellent cycling stability. Clearly, the redox reactions of the MoS_6 and MoS_6@15%$Li_7P_3S_{11}$ composite occur within the potential window of 1.0–3.0 V, which was selected to further evaluate electrochemical performances.

Figure 4c,d present the galvanostatic discharge–charge curves of the first three cycles of the MoS_6 and MoS_6@15% $Li_7P_3S_{11}$ composite in the all-solid-state lithium batteries at 0.1 A g^{-1} and 25 °C. The all-solid-sate lithium battery with the MoS_6 cathodes delivered a high initial discharge capacity of 913.9 mAh g^{-1}. After coupling with the $Li_7P_3S_{11}$ solid-electrolyte thin layer, the all-solid-state lithium battery with the MoS_6@15%$Li_7P_3S_{11}$ composite cathodes delivered initial and reversible discharge capacities of 1083.8 mAh g^{-1} and 851.5 mAh g^{-1}, respectively (Figure 4d), which were the one of highest values observed among the many sulfide-based cathode materials, i.e., rGO-MoS_3, cubic FeS_2, Co_9S_8@$Li_7P_3S_{11}$, and MoS_2@$Li_7P_3S_{11}$ [10,17,19,21]. As is shown in Table S2, the initial discharge capacities of the rGO-MoS_3, FeS_2, Co_9S_8@$Li_7P_3S_{11}$, and MoS_2@$Li_7P_3S_{11}$ were 1241.4 mAh g^{-1}, 750 mAh g^{-1}, 633 mAh g^{-1}, and 868.4 mAh g^{-1}, respectively, while their respective reversible capacities were around 760 mAh g^{-1}, 730 mAh g^{-1}, 574 mAh g^{-1}, and 669.2 mAh g^{-1}. The increased reversible discharge capacity compared with that of the MoS_6 could be attributed to the better interface compatibility between the active material and the solid electrolyte. In addition, the initial Coulombic efficiency of the MoS_6@15%$Li_7P_3S_{11}$ composite was 73.2%, which was higher than that of the MoS_6 (65.6%). These values were calculated using the equation $Coulombic\ efficiency = \frac{C_{charge}}{C_{discharge}}$, where C is the specific capacity of the charge or discharge process. As is shown in Figure 4e, the MoS_6@15%$Li_7P_3S_{11}$ composite exhibited a remarkably stable cyclic performance with an impressive reversible specific capacity of 693.2 mAh g^{-1} after 20 cycles, while the MoS_6 only showed a reversible specific capacity of 517.7 mAh g^{-1}. The excellent electrochemical performance of the MoS_6@15%$Li_7P_3S_{11}$ composite can be attributed to the $Li_7P_3S_{11}$ thin layer, which can improve the cathode–electrolyte compatibility. In fact, the coating ratio of the $Li_7P_3S_{11}$ solid electrolyte also affected the electrochemical performance of the MoS_6@$Li_7P_3S_{11}$ composite (Figure S4). The Li/Li_6PS_5Cl/MoS_6@10%$Li_7P_3S_{11}$ and Li/Li_6PS_5Cl/MoS_6@20%$Li_7P_3S_{11}$ delivered initial discharges of 967.8 mAh g^{-1} and 991.4 mAh g^{-1}, respectively. After 20 cycles, the capacity retention values of the 10%$Li_7P_3S_{11}$- and 20%$Li_7P_3S_{11}$-coated electrodes were 476.1 mAh g^{-1} and 496.3 mAh g^{-1}, respectively. Obviously, the Li/Li_6PS_5Cl/MoS_6@15%$Li_7P_3S_{11}$ displayed the highest reversible capacity. To explore the principles of cathode kinetics and capacity variation for the Li/Li_6PS_5Cl/MoS_6 and Li/Li_6PS_5Cl/MoS_6@15%$Li_7P_3S_{11}$ all-solid-state lithium batteries, EIS was conducted with an amplitude of 15 mV from 10^6 to 0.1 Hz. The corresponding equivalent circuit model is shown in Figure 4f, in which R_e is the resistance of the electrolyte, the semicircle shows the emergence of the interfacial charge transfer resistance (R_{ct}), the constant phase angle element (CPE) is used to indicate the behavior of the non-ideal capacitance of the double-layer, and Z_w represents the Warburg resistance, which indicates that the lithium ions diffuse into the bulk electrodes [21,28]. The fitted R_e and R_{ct} results are listed in Table S3. After the first cycle, the EIS plots of the MoS_6 and MoS_6@15%$Li_7P_3S_{11}$ composite-based all-solid-state lithium batteries were straight lines. The MoS_6@15%$Li_7P_3S_{11}$ composite exhibited an R_e value of 75.89 Ω, which was lower than that of the MoS_6 (105.42 Ω). After 20 cycles, the MoS_6

exhibited higher R_e (384.11 Ω) and R_{ct} (52.96 Ω) values. In contrast, the MoS_6@15%$Li_7P_3S_{11}$ composite exhibited respective R_e and R_{ct} values of 124.79 Ω and 10.78 Ω due to the intimate interfacial contact.

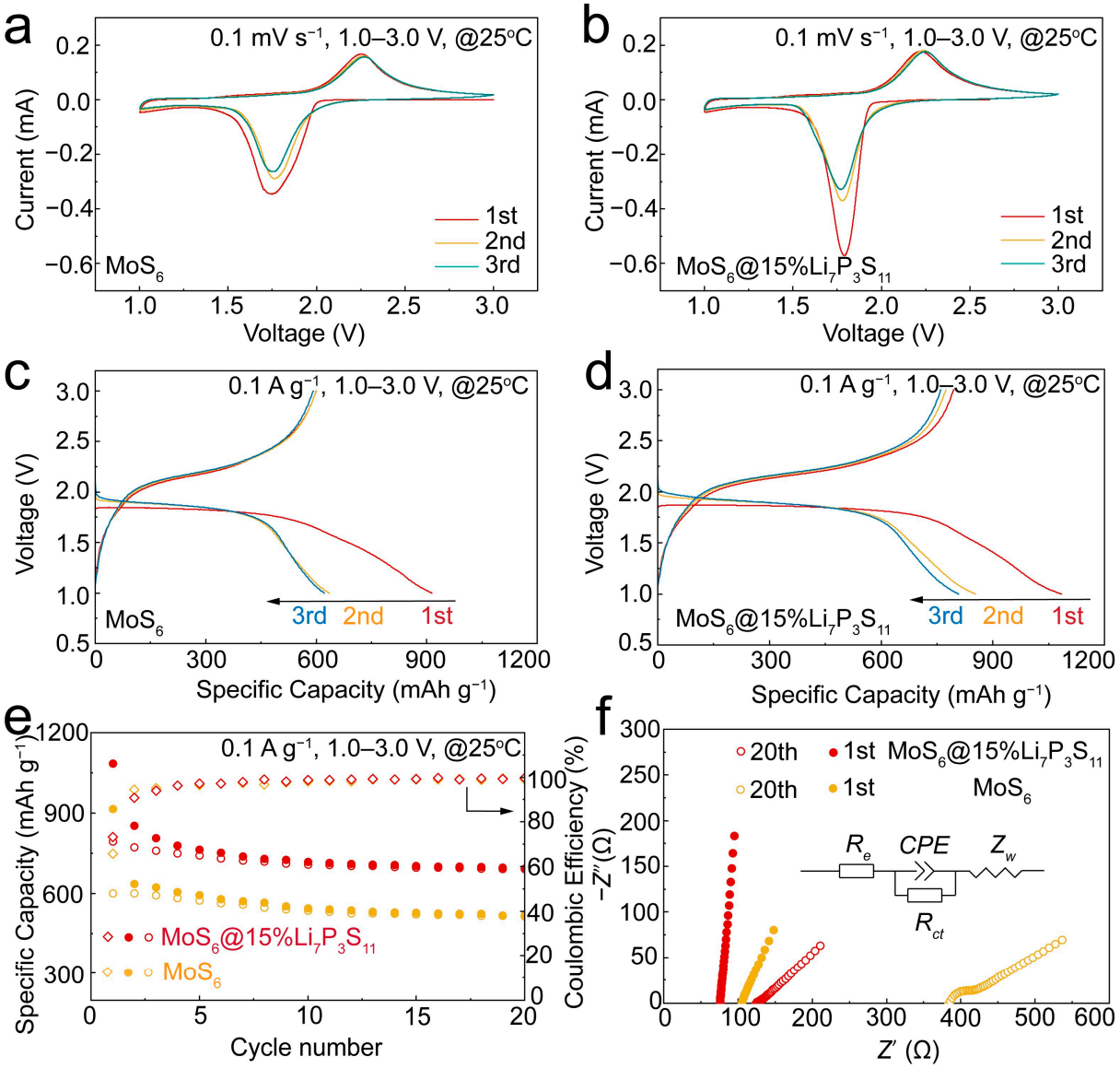

Figure 4. CV curves of (**a**) MoS_6 and (**b**) MoS_6@15%$Li_7P_3S_{11}$ composite; galvanostatic discharge/charge profiles of (**c**) MoS_6 and (**d**) MoS_6@15%$Li_7P_3S_{11}$ composite cathodes at 0.1 A g^{-1}; (**e**) cyclic performances of MoS_6 and MoS_6@15%$Li_7P_3S_{11}$ composite at 0.1 A g^{-1} within 1.0–3.0 V (the solid circles represent discharge capacities); (**f**) Nyquist plots and equivalent circuit diagram of MoS_6 and MoS_6@15%$Li_7P_3S_{11}$ composite cathodes after 1st and 20th cycles at 0.1 A g^{-1} within 1.0–3.0 V.

The rate capabilities of the MoS_6 and MoS_6@15%$Li_7P_3S_{11}$ composite cathodes were measured under various current densities ranging from 0.1 to 2 A g^{-1} (Figure 5a). The MoS_6@15%$Li_7P_3S_{11}$ composite cathodes exhibited superior reversible discharge capacities of 801.5, 648.1, 536.3, 454.4, and 370.8 mAh g^{-1} under current densities of 0.1, 0.2, 0.5, 1, and 2 A g^{-1}, respectively, while the MoS_6 only exhibited reversible discharge capacities 683.9, 516.8, 407.7, 326.2, and 255.8 mAh g^{-1}. The excellent rate capability of the MoS_6@15%$Li_7P_3S_{11}$ composite can be attributed to its enhanced ionic diffusivity, which led to improved electrochemical reaction kinetics. The Ragone plot shown in Figure 5b gives the relationship between the average power density and energy density. The power density of the MoS_6 and MoS_6@15%$Li_7P_3S_{11}$ composite were calculated using the equation

$power\ density = \frac{ED \times \frac{m_{active\ materials}}{m_{cathode\ layer}}}{t}$, where ED is the energy density of the active materials, m is the loading weight of the active materials or the cathode layer, and t is the duration of the discharge process. The MoS_6 and MoS_6@15%$Li_7P_3S_{11}$ composite numbers that were used in the energy density and power density calculations are listed in Tables S4 and S5. At current densities of 0.1 and 2.0 A g^{-1}, the MoS_6@15%$Li_7P_3S_{11}$ composite cathodes delivered energy and power densities of 588 Wh kg^{-1} and 1358 W kg^{-1}, respectively, based on the total cathode layer which is composed of the MoS_6@15%$Li_7P_3S_{11}$ composite, $Li_{10}GeP_2S_{12}$, and super P. These values were significantly higher than the energy and power densities of 495.8 Wh kg^{-1} and 1332.2 W kg^{-1} exhibited by the MoS_6 at the same respective current densities. The long-term cycling stability of the MoS_6@15%$Li_7P_3S_{11}$ composite cathodes at 1 A g^{-1} is further shown in Figure 5c, which shows that the cathodes exhibited a high reversible capacity of 400 mAh g^{-1} after 1000 cycles.

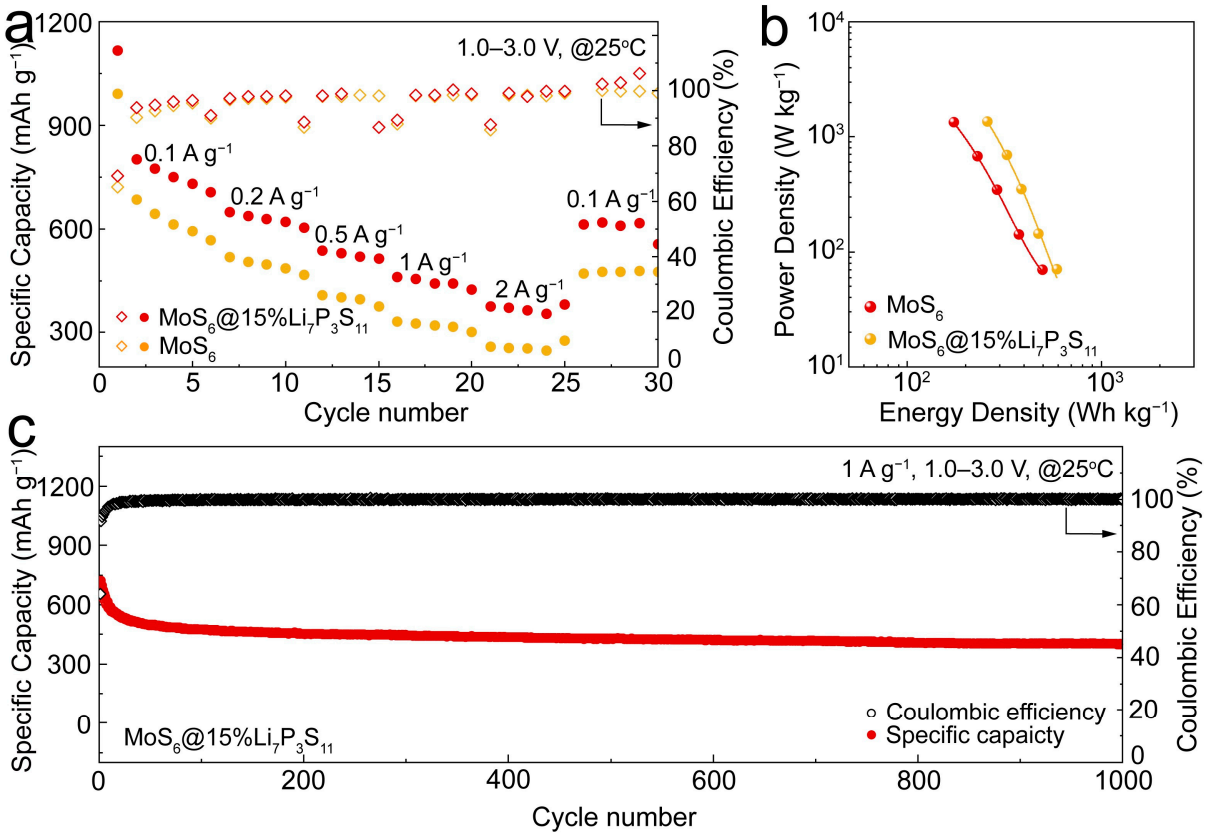

Figure 5. (**a**) Rate performances of MoS_6 and MoS_6@15%$Li_7P_3S_{11}$ composite under different current densities. (**b**) Ragone plot deduced from the rate performances shown in (**a**). (**c**) Long-term cyclic performance of MoS_6@15%$Li_7P_3S_{11}$ composite at 1 A g^{-1}.

CV measurements were conducted to illustrate the electrochemical reaction kinetics. The relationship between the peak current (i) and the scan rate obeys the power law: $i = av^b$. The b-value is fitted using a log(v)-log(i) plot. A b-value of 1.0 indicates a surface-mediated mode, while a b-value of 0.5 indicates a diffusion-controlled mode. The CV curves shown in Figure 6a,c show similar shapes and gradually broadened redox peaks. At the same scan rate, the curve intensity of the MoS_6@15%$Li_7P_3S_{11}$ composite was higher than that of the MoS_6, indicating that the MoS_6@15%$Li_7P_3S_{11}$ composite can maintain fast electrochemical kinetics with an increased scan rate. As shown in Figure 6b, the fitted b-values of the reduction peak and the oxidation peak were 0.50 and 0.67, respectively, for the MoS_6@15%$Li_7P_3S_{11}$ composite; these values are lower than the fitted b-values of 0.62 and 0.76 recorded for the MoS_6 (Figure 6d), indicating that the electrochemical reaction

kinetics are dominated by diffusion-controlled processes. This condition allows lithium ions to become fully intercalated and thereby realize high reversible capacity [17,29].

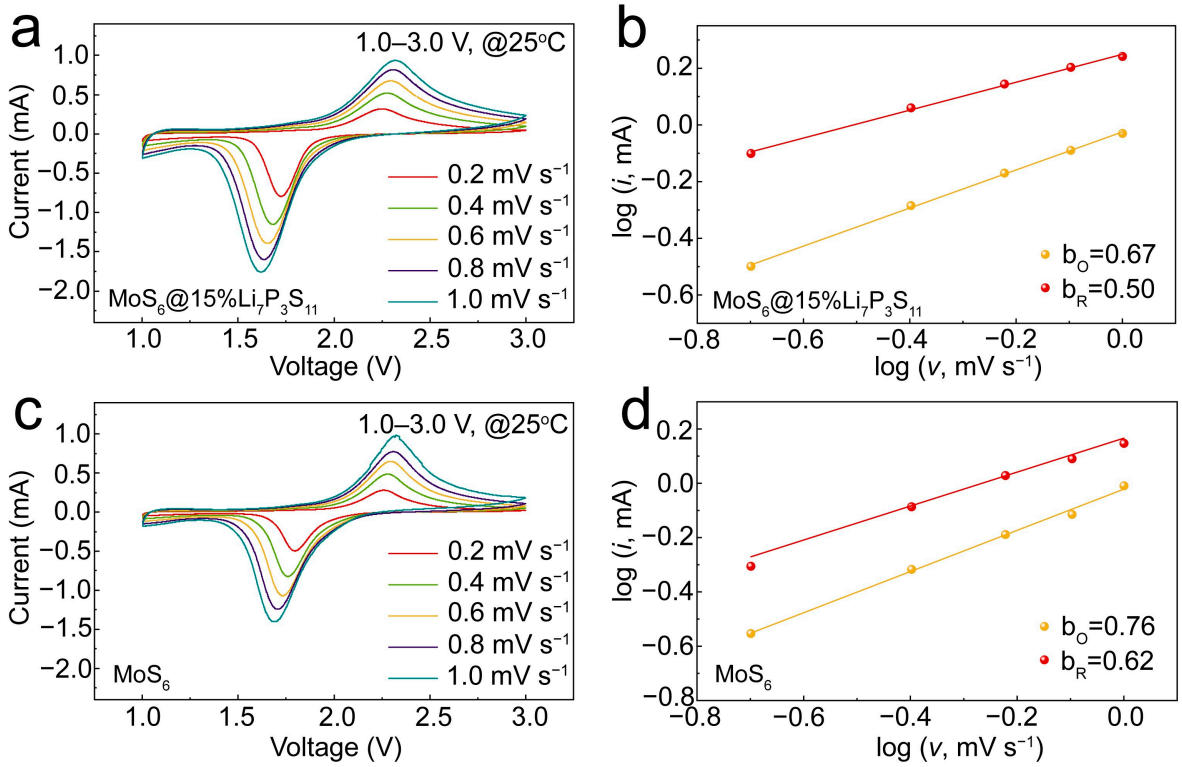

Figure 6. CV curves at different scan rates for (**a**) MoS_6@15%$Li_7P_3S_{11}$ composite and (**c**) MoS_6. The log (peak current) vs. log (scan rate) fitted plots at reduction and oxidation peaks of (**b**) MoS_6@15%$Li_7P_3S_{11}$ composite and (**d**) MoS_6.

To further quantify the ionic transport kinetics of the Li/Li_6PS_5Cl/MoS_6@15%$Li_7P_3S_{11}$ and Li/Li_6PS_5Cl/MoS_6 all-solid-state batteries, the GITT was used and calculated were made to determine the lithium ion diffusion coefficients at 1 A g^{-1} and 1.0–3.0 V. As is shown in Figure 7, the ion diffusion coefficient range of the MoS_6@15%$Li_7P_3S_{11}$ composite was calculated to be 10^{-11}–10^{-10} cm^2 s^{-1}, which is higher than that of the MoS_6 (10^{-12}–10^{-11} cm^2 s^{-1}). Obviously, the ionic diffusivity of the MoS_6@15%$Li_7P_3S_{11}$ composite was enhanced significantly; this is beneficial for the rapid transportation of lithium ions and thus significantly improved the electrochemical performances related to high discharge capacity and rate capability.

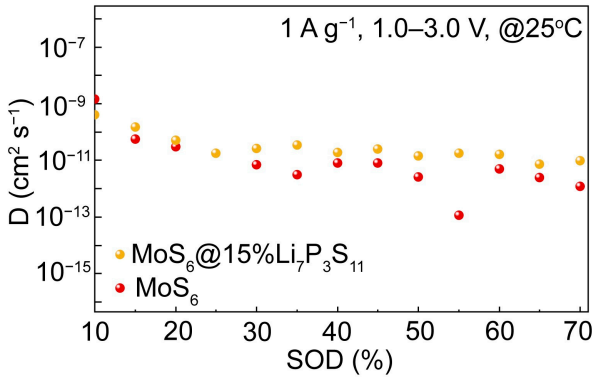

Figure 7. GITT plot of Li/Li_6PS_5Cl/MoS_6@15%$Li_7P_3S_{11}$ composite and Li/Li_6PS_5Cl/MoS_6 all-solid-state lithium batteries.

4. Conclusions

In summary, the micro-sized MoS_6 with high S_2^{2-} content demonstrated a high initial theoretical capacity of 1117 mAh g^{-1}. After coating the MoS_6 with $Li_7P_3S_{11}$ solid electrolytes, the resulting MoS_6@15%$Li_7P_3S_{11}$ composite was able to achieve an improved ion diffusion coefficient range of 10^{-11}–10^{-10} cm^2 s^{-1}, which was higher than the value of the MoS_6 (10^{-12}–10^{-11} cm^2 s^{-1}). The Li/Li_6PS_5Cl/MoS_6@15%$Li_7P_3S_{11}$ all-solid-sate lithium batteries showed a high initial discharge capacity of 1083.8 mAh g^{-1} at 0.1 A g^{-1} and a long cycle life of 1000 cycles at 1A g^{-1} and 25 °C. In addition, the MoS_6@15%$Li_7P_3S_{11}$ composite displayed a high energy density of 588 Wh kg^{-1} and a power density of 1358 W kg^{-1} based on the total cathode layer. This contribution provides a new sulfide-based cathode material with high specific capacity and a superior ion diffusion coefficient which has promising application potential for use in all-solid-state lithium batteries.

Supplementary Materials: The follow supporting information can be downloaded at: https://www.mdpi.com/article/10.3390/batteries9110560/s1, Figure S1: XRD pattern of $(NH_4)_2Mo_2S_{12}$; Figure S2: Cyclic performances of Li/Li_6PS_5Cl/MoS_6 and Li/75%Li_2S-24%P_2S_5-1%P_2O_5/$Li_{10}GeP_2S_{12}$/MoS_6 all-solid-state batteries under 0.2 A g^{-1}; Figure S3: Cyclic performances of all-solid-state batteries with 50MoS_6:50$Li_{10}GeP_2S_{12}$, 40MoS_6:50$Li_{10}GeP_2S_{12}$:10Super P, and 40MoS_6:40$Li_{10}GeP_2S_{12}$:20Super P cathodes under 0.1 A g^{-1}; Figure S4: Cyclic performances of MoS_6@10%$Li_7P_3S_{11}$, MoS_6@15%$Li_7P_3S_{11}$, and MoS_6@20%$Li_7P_3S_{11}$ cathodes under 0.1 A g^{-1}; Table S1: Inductively coupled plasma emission spectrometer analysis of MoS_6; Table S2: Electrochemical performances comparisons of various active materials in all-solid-state-batteries; Table S3: EIS fitting results of MoS_6 and MoS_6@15%$Li_7P_3S_{11}$ under 0.1 A g^{-1} after 20 cycles; Table S4: MoS_6 values used in energy density and power density calculations; Table S5: MoS_6@15%$Li_7P_3S_{11}$ composite values used in energy density and power density calculations.

Author Contributions: Conceptualization: X.Y.; methodology: M.C. and X.Y.; general experimental investigation and electrochemical analysis: M.C., M.Y., W.X., F.T. and G.L.; characterization: M.C.; supervision and research guidance: P.C., T.W. and X.Y.; funding acquisition: X.Y. All authors have read and agreed to the published version of the manuscript.

Funding: This work was supported by National Natural Science Foundation of China (Grant No. U1964205), the Jiangsu Provincial S&T Innovation Special Programme for Carbon Peak and Carbon Neutrality (Grant No. BE2022007), and the Youth Innovation Promotion Association CAS (Y2021080).

Data Availability Statement: The data presented in this study are available on request from the corresponding author. The data are not publicly available due to privacy policy.

Conflicts of Interest: The authors declare no conflict of interest.

References

1. Zhao, W.G.; Zou, L.F.; Jia, H.P.; Zheng, J.M.; Wang, D.H.; Song, J.H.; Hong, C.Y.; Liu, R.; Xu, W.; Yang, Y.; et al. Optimized Al Doping Improves Both Interphase Stability and Bulk Structural Integrity of Ni-Rich NMC Cathode Materials. *ACS Appl. Energy Mater.* **2020**, *3*, 3369–3377. [CrossRef]
2. Bruce, P.G.; Freunberger, S.A.; Hardwick, L.J.; Tarascon, J.M. Li-O_2 and Li-S batteries with high energy storage. *Nat. Mater.* **2012**, *11*, 19–29. [CrossRef]
3. Kato, Y.; Hori, S.; Saito, T.; Suzuki, K.; Hirayama, M.; Mitsui, A.; Yonemura, M.; Iba, H.; Kanno, R. High-power all-solid-state batteries using sulfide superionic conductors. *Nat. Energy* **2016**, *1*, 16030. [CrossRef]
4. Yi, Y.K.; Hai, F.; Guo, J.Y.; Tian, X.L.; Zheng, S.T.; Wu, Z.D.; Wang, T.; Li, M.T. Progress and Prospect of Practical Lithium-Sulfur Batteries Based on Solid-Phase Conversion. *Batteries* **2023**, *9*, 27. [CrossRef]
5. Shi, C.M.; Alexander, G.V.; O'Neill, J.; Duncan, K.; Godbey, G.; Wachsman, E.D. All-Solid-State Garnet Type Sulfurized Polyacrylonitrile/Lithium-Metal Battery Enabled by an Inorganic Lithium Conductive Salt and a Bilayer Electrolyte Architecture. *ACS Energy Lett.* **2023**, *8*, 1803–1810. [CrossRef]
6. Kamaya, N.; Homma, K.; Yamakawa, Y.; Hirayama, M.; Kanno, R.; Yonemura, M.; Kamiyama, T.; Kato, Y.; Hama, S.; Kawamoto, K.; et al. A lithium superionic conductor. *Nat. Mater.* **2011**, *10*, 682–686. [CrossRef] [PubMed]
7. Boulineau, S.; Courty, M.; Tarascon, J.M.; Viallet, V. Mechanochemical synthesis of Li-argyrodite Li_6PS_5X (X = Cl, Br, I) as sulfur-based solid electrolytes for all solid state batteries application. *Solid State Ion.* **2012**, *221*, 1–5. [CrossRef]
8. Grayfer, E.D.; Pazhetnov, E.M.; Kozlova, M.N.; Artemkina, S.B.; Fedorov, V.E. Anionic Redox Chemistry in Polysulfide Electrode Materials for Rechargeable Batteries. *ChemSusChem* **2017**, *10*, 4805–4811. [CrossRef]

9. Sakuda, A.; Ohara, K.; Fukuda, K.; Nakanishi, K.; Kawaguchi, T.; Arai, H.; Uchimoto, Y.; Ohta, T.; Matsubara, E.; Ogumi, Z.; et al. Amorphous Metal Polysulfides: Electrode Materials with Unique Insertion/Extraction Reactions. *J. Am. Chem. Soc.* **2017**, *139*, 8796–8799. [CrossRef]
10. Yersak, T.A.; Macpherson, H.A.; Kim, S.C.; Le, V.D.; Kang, C.S.; Son, S.B.; Kim, Y.H.; Trevey, J.E.; Oh, K.H.; Stoldt, C.; et al. Solid State Enabled Reversible Four Electron Storage. *Adv. Energy Mater.* **2013**, *3*, 120–127. [CrossRef]
11. Wang, T.S.; Hu, P.; Zhang, C.J.; Du, H.P.; Zhang, Z.H.; Wang, X.G.; Chen, S.G.; Xiong, J.W.; Cui, G.L. Nickel Disulfide-Graphene Nanosheets Composites with Improved Electrochemical Performance for Sodium Ion Battery. *ACS Appl. Mater Interfaces* **2016**, *8*, 7811–7817. [CrossRef]
12. Arsentev, M.; Missyul, A.; Petrov, A.V.; Hammouri, M. TiS_3 Magnesium Battery Material: Atomic-Scale Study of Maximum Capacity and Structural Behavior. *J. Phys. Chem. C* **2017**, *121*, 15509–15515. [CrossRef]
13. Dong, S.W.; Sheng, L.; Wang, L.; Liang, J.; Zhang, H.; Chen, Z.H.; Xu, H.; He, X.M. Challenges and Prospects of All-Solid-State Electrodes for Solid-State Lithium Batteries. *Adv. Funct. Mater.* **2023**, 2304371. [CrossRef]
14. Chong, P.D.; Zhou, Z.W.; Wang, K.H.; Zhai, W.H.; Li, Y.F.; Wang, J.B.; Wei, M.D. The Stabilizing of 1T-MoS_2 for All-Solid-State Lithium-Ion Batteries. *Batteries* **2023**, *9*, 26. [CrossRef]
15. Wang, Y.F.; Goikolea, E.; de Larramendi, I.R.; Lanceros-Méndez, S.; Zhang, Q. Recycling methods for different cathode chemistries—A critical review. *J. Energy Storage* **2022**, *56*, 106053. [CrossRef]
16. Shchegolkov, A.V.; Komarov, F.F.; Lipkin, M.S.; Milchanin, O.V.; Parfimovich, I.D.; Shchegolkov, A.V.; Semenkova, A.V.; Velichko, A.V.; Chebotov, K.D.; Nokhaeva, V.A. Synthesis and Study of Cathode Materials Based on Carbon Nanotubes for Lithium-Ion Batteries. *Inorg. Mater. Appl. Res.* **2021**, *12*, 1281–1287. [CrossRef]
17. Zhang, Q.; Ding, Z.G.; Liu, G.Z.; Wan, H.L.; Mwizerwa, J.P.; Wu, J.H.; Yao, X.Y. Molybdenum trisulfide based anionic redox driven chemistry enabling high-performance all-solid-state lithium metal batteries. *Energy Storage Mater.* **2019**, *23*, 168–180. [CrossRef]
18. Wu, F.X.; Yushin, G. Conversion cathodes for rechargeable lithium and lithium-ion batteries. *Energy Environ. Sci.* **2017**, *10*, 435–459. [CrossRef]
19. Xu, R.C.; Wang, X.L.; Zhang, S.Z.; Xia, Y.; Xia, X.H.; Wu, J.B.; Tu, J.P. Rational coating of $Li_7P_3S_{11}$ solid electrolyte on MoS_2 electrode for all-solid-state lithium ion batteries. *J. Power Sources* **2018**, *374*, 107–112. [CrossRef]
20. Ye, H.; Ma, L.; Zhou, Y.; Wang, L.; Han, N.; Zhao, F.; Deng, J.; Wu, T.; Li, Y.; Lu, J. Amorphous MoS_3 as the sulfur-equivalent cathode material for room-temperature Li-S and Na-S batteries. *Proc. Natl. Acad. Sci. USA* **2017**, *114*, 13091–13096. [CrossRef]
21. Yao, X.; Liu, D.; Wang, C.; Long, P.; Peng, G.; Hu, Y.S.; Li, H.; Chen, L.; Xu, X. High-Energy All-Solid-State Lithium Batteries with Ultralong Cycle Life. *Nano Lett.* **2016**, *16*, 7148–7154. [CrossRef] [PubMed]
22. Ye, H.L.; Wang, L.; Deng, S.; Zeng, X.Q.; Nie, K.Q.; Duchesne, P.N.; Wang, B.; Liu, S.; Zhou, J.H.; Zhao, F.P.; et al. Amorphous MoS_3 Infiltrated with Carbon Nanotubes as an Advanced Anode Material of Sodium-Ion Batteries with Large Gravimetric, Areal, and Volumetric Capacities. *Adv. Energy Mater.* **2017**, *7*, 160102. [CrossRef]
23. Wang, X.; Du, K.; Wang, C.; Ma, L.; Zhao, B.; Yang, J.; Li, M.; Zhang, X.X.; Xue, M.; Chen, J. Unique Reversible Conversion-Type Mechanism Enhanced Cathode Performance in Amorphous Molybdenum Polysulfide. *ACS Appl. Mater. Interfaces* **2017**, *9*, 38606–38611. [CrossRef] [PubMed]
24. Horner, J.S.; Whang, G.; Ashby, D.S.; Kolesnichenko, I.V.; Lambert, T.N.; Dunn, B.S.; Talin, A.A.; Roberts, S.A. Electrochemical Modeling of GITT Measurements for Improved Solid-State Diffusion Coefficient Evaluation. *ACS Appl. Energy Mater.* **2021**, *4*, 11460–11469. [CrossRef]
25. Shen, Z.; Cao, L.; Rahn, C.D.; Wang, C.Y. Least Squares Galvanostatic Intermittent Titration Technique (LS-GITT) for Accurate Solid Phase Diffusivity Measurement. *J. Electrochem. Soc.* **2013**, *160*, A1842–A1846. [CrossRef]
26. Mabayoje, O.; Wygant, B.R.; Wang, M.; Liu, Y.; Mullins, C.B. Sulfur-Rich MoS_6 as an Electrocatalyst for the Hydrogen Evolution Reaction. *ACS Appl. Energy Mater.* **2018**, *1*, 4453–4458. [CrossRef]
27. Tran, P.D.; Tran, T.V.; Orio, M.; Torelli, S.; Truong, Q.D.; Nayuki, K.; Sasaki, Y.; Chiam, S.Y.; Yi, R.; Honma, I.; et al. Coordination polymer structure and revisited hydrogen evolution catalytic mechanism for amorphous molybdenum sulfide. *Nat. Mater.* **2016**, *15*, 640–646. [CrossRef]
28. Huang, J. Diffusion impedance of electroactive materials, electrolytic solutions and porous electrodes: Warburg impedance and beyond. *Electrochim. Acta* **2018**, *281*, 170–188. [CrossRef]
29. Li, W.B.; Huang, J.F.; Cao, L.Y.; Feng, L.L.; Yao, C.Y. Controlled construction of 3D self-assembled VS_4 nanoarchitectures as high-performance anodes for sodium-ion batteries. *Electrochim. Acta* **2018**, *274*, 334–342. [CrossRef]